J Mater Sci (2009) 44:3889–3899
DOI 10.1007/s10853-009-3531-7

Shape-selective synthesis and opto-electronic properties of Eu^{3+}-doped gadolinium oxysulfide nanostructures

J. Thirumalai · R. Chandramohan · S. Valanarasu · T. A. Vijayan · R. M. Somasundaram · T. Mahalingam · S. R. Srikumar

Received: 5 February 2009 / Accepted: 29 April 2009 / Published online: 15 May 2009

Abstract A simple and facile hydrothermal route has been demonstrated for the shape-selective preparation of highly crystalline $Gd_2O_2S:Eu^{3+}$ nanostructures, such as nanocrystals/nanoplates, nanosheets, nanobelts, nanotubes, nanorods, and nanowires are characterized by X-ray diffraction (XRD), scanning electron microscopy (SEM), and transmission electron microscopy (TEM), photoluminescence (PL) techniques. The as-prepared samples are characterized using X-ray photoelectron spectra (XPS), to investigate the elementary states on the surfaces. The concentration of precursor chemicals, pH, the reaction time, and the temperature are important factors in the morphological control of $Gd_2O_2S:Eu^{3+}$ nanostructures. The adjustment of these parameters can lead to an obvious shape evolution of products. The origin and nature of the opto-electronic transitions were observed using opto-impedance measurements.

J. Thirumalai · R. Chandramohan (✉) · T. A. Vijayan
Department of Physics, Sree Sevugan Annamalai College, Devakottai 630 303, Tamil Nadu, India
e-mail: chandramohan_rm@rediffmail.com

S. Valanarasu
Department of Physics, Ananda College, Devakottai 630 303, Tamil Nadu, India

R. M. Somasundaram
Department of Chemistry, Sree Sevugan Annamalai College, Devakottai 630 303, Tamil Nadu, India

T. Mahalingam
School of Physics, Alagappa University, Karaikudi 630 003, Tamil Nadu, India

S. R. Srikumar
Department of Physics, Kalasalingam University, Krishnankoil 626 190, Tamil Nadu, India

Introduction

The well-defined shape control of inorganic semiconductor nanostructures has attracted considerable attention for potential applications due to their physical and chemical properties, which are determined by morphology, size, and dimensions [1–5]. Thus, the shape control of semiconductor nanostructures has been the topic of intensive investigation in recent materials science. The interest in nanoscale materials stems from the fact that new properties are acquired at this length scale and, equally important, that these properties change with their size or shape. The change in the properties at this length scale is not a result of scaling factors. It results from different causes in different materials. The ability to control and manipulate the physical and chemical properties of materials, as we desire is one of the challenging issues in chemistry and materials science. Modern chemists are now exploring ways to obtain such control at the nanometer scale. Recent years have seen considerable interest in the fabrication of low-dimensional nanosized materials, such as nanosheets, nanobelts, nanotubes, nanorods, and nanowires while collections of nanostructures involve arrays, assemblies, and superlattices [6–8]. As suggested from the unique combination of optoelectronic, mechanical, and chemical properties of oxysulfide nanocrystals (quantum-dots), nanotubes [9–11], nanotubular materials are expected to have unusual characteristics amplified by their marked shape-specific and size effects.

By controlling the reaction parameters such as molar ratio between capping agent and metallic precursor, temperature, reaction time and the order of addition of reactants, a reasonable control of the size and morphology can be achieved [12, 13]. In recent years, lanthanide-doped luminescent nano-sized materials have received much

attention for their wide applications on high-resolution displays, integrated optical systems, substitute for organic dyes, solid-state lasers, and especially biological labels. Trivalent europium-doped gadolinium oxysulfide (band gap ~4.2–4.8 eV) is an important phosphor system extensively applied in color televisions, display devices, electronic portal imaging device (EPID), radioisotope distribution and so on [14–16]. In addition to the conventional vapor-phase methods of vapor transport and condensation [17–22], thermal evaporation [23, 24] and metal-organic chemical vapor deposition [25] solution-phase methods have been developed as alternative ways to synthesize semiconductor nanostructures with different shapes and dimensions. Hydrothermal [26, 27] is a widely used technique that can control the shape and dimension of nanostructures among all solution-based approaches. Unlike conventional vapor-phase methods, the hydrothermal method can produce various nanostructures at a relatively low temperature (below 200 °C) using simple equipments; however, the reaction time required for the growth of nanostructures is too long (usually from a few hours to several days [3, 26, 27]. Therefore, the development of a simple and fast synthetic route that can control the shape of nanostructures under ambient conditions remained an important topic of investigation.

The hydrothermal method has been recently investigated as a promising alternative technique for the fabrication of hydroxide and oxysulfide nanomaterials under ambient conditions [10, 28, 29]. The reason is that this method is fast, simple, economical, and environment friendly [30–32]. In this hydrothermal synthesis of $Gd_2O_2S:Eu^{3+}$ nanostructures with different shapes have not yet been reported. In this article, as a continuation of our research in this field, we have controllably prepared single crystalline $Gd_2O_2S:Eu^{3+}$ with various morphologies nanocrystals/nanoplates, nanosheets, nanobelts, nanotubes, nanorods, and nanowires via the hydrothermal process. It is shown that this is a simple, mild, and efficient approach for the controlled growth of $Gd_2O_2S:Eu^{3+}$ materials with different morphologies. The influences of experimental conditions (temperature, reactant ratio, and pH) on the final morphologies of products are investigated in detail, and the corresponding crystal growth mechanism has been proposed. Owing to the excellent novel properties of the rare-earth compounds, the doped oxysulfide nanostructures may find applications in optoelectronics, nanoscale devices, low-dimensional physics and materials science, biological technology and molecular catalysts. The method presented here possesses several advantages, including high yields, high purities, low cost, and environmental benignity. It might feasibly be ease of scale-up for industrial mass production. We believe this technique will be readily adopted in realizing other forms of various nanostructured materials.

Experimental section

All reagents were analytical grade and were used without further purification in the experiment. The preparation of $Gd_2O_2S:Eu^{3+}$ nanostructures are similar to the method reported by our group [10]. Using the same synthesis procedure various nanostructures such as nanocrystals, nanosheets, nanobelts nanotubes, nanorods, and nanowires are synthesized here. In a typical synthesis, 0.9 mM of $Gd(NO_3)_3 \cdot 6H_2O$ were dissolved in deionized water to form a clear solution and the pH of the solution was adjusted to 7–13 by adding NaOH solution under vigorous stirring. The mixture was then transferred to a Teflon lined stainless steel autoclave and heated at 100–180 °C for 12–48 h. A white precipitate was collected, purified, and dried in air at ambient temperature. The as-prepared $Gd(OH)_3$ nanostructures were first dispersed into (0.1 mM) of $Eu(NO_3)_3 \cdot 6H_2O$ aqueous solutions, then stirred for 2 h at 70–80 °C, followed by a subsequent sulfuration process under a vigorous stirring that leads to doped Gd(OH) nanostructures that could further be converted to the formation of Eu^{3+}-doped gadolinium oxysulfide ($Gd_2O_2S:Eu^{3+}$) nanocrystals, nanosheets, nanobelts nanotubes, nanorods, and nanowires at 600 °C for 2 h under inert (Ar or N_2)/CS_2/Sulfur/Carbon atmosphere. For comparison purposes polycrystalline $Gd_2O_2S:Eu^{3+}$ (sample B) was prepared through a conventional solid-state reaction method [10]. The detailed experimental parameters together with the morphological properties of the corresponding products (denoted as B1 to B12) are listed in Table 1. For comparison purposes polycrystalline $Gd_2O_2S:Eu^{3+}$ (sample B) was prepared through a conventional solid-state reaction method [9, 10]. The X–ray diffraction (XRD) patterns were recorded on Philips X'Pert PRO system from PanAlytical diffractometer with Cu Kα radiation ($\lambda = 0.15406$ nm) and a scanning rate of $\overset{\circ}{5}$ min^{-1}. Transmission electron microscopy (TEM), high-resolution transmission electron microscopy (HRTEM), and selected area electron diffraction (SAED) were taken with a JEOL JEM–2010F operated at 200 kV (JEOL, Japan). Samples for TEM were prepared by dropping a diluted suspension of the sample powders onto a standard carbon-coated (20–30 nm) film on a copper grid (230 mesh) and air-dried. XPS measurements were performed using a LAS-3000 surface analysis system (RIBER, France) and AlKα X-rays (1489.6 eV, width 0.5 eV). Room temperature photoluminescence (PL) spectra were recorded with a VARIAN Cary Eclipse spectrophotometer equipped with a 150 W xenon lamp as the excitation source. Photo-induced impedance measurements were carried out using SOLATRON instrument on both dark and UV (254 and 365 nm) shined conditions. The as-synthesized powder samples were made by compacting the powder samples to solid discs at ~10 mm diameter and 1 mm thickness and

Table 1 Optimal experimental conditions and resulting morphologies $Gd(OH)_3$ and $Gd_2O_2S:Eu^{3+}$ nanostructures

S. No.	Sample		Experimental conditions			Resulting morphologies	
			T (°C)	pH	t (h)	Shape	Size
1.	$Gd(OH)_3$	B_1	100	~7–8	48	Hexagonal/spherical Nanocrystals	≈15–20 nm (Spherical) ≈25–30 nm (Hexagonal)
		B_2	140	~7–8	~12	Nanosheets	$t \approx 15$ nm, $W \approx 100$ nm
		B_3	180	~8	24	Nanobelts	$t \approx 20$ nm, $L \leq 2$ μm
		B_4	120–140	~12–13	24	Nanotubes	$D \approx 20$ nm, $L \approx 200$ nm
		B_5	140–160	~12	24	Nanorods	$D \approx 15$ nm, $L \approx 100$ nm
		B_6	180	~9	48	Nanowires	$D \approx 15$ nm, $L \geq 200$ nm
2.	$Gd_2O_2S:Eu^{3+}$	B_7	–	–	–	Hexagonal/spherical Nanocrystals	≈15 nm (Spherical) ≈20–30 nm (Hexagonal)
		B_8	–	–	–	Nanosheets	$t \approx 15$ nm, $W \approx 80$ nm
		B_9	–	–	–	Nanobelts	$t \approx 25$ nm, $L \leq 2$ μm
		B_{10}	–	–	–	Nanotubes	$D \approx 15$ nm, $L \approx 200$ nm
		B_{11}	–	–	–	Nanorods	$D \approx 15$ nm, $L \approx 100$ nm
		B_{12}	–	–	–	Nanowires	$D \leq 15$ nm, $L \geq 250$ nm

"–" represents the formation of $Gd_2O_2S:Eu^{3+}$nanostructures synthesized at 600 °C, 2 h converted using the experimental conditions of $Gd(OH)_3$ nanostructures

the pellet/disc is held across the silver contacts like a two–electrode system. All the measurements were performed at room temperature.

Results and discussion

Structure and morphology of $Gd_2O_2S:Eu^{3+}$ nanostructures

The purity and crystallinity of the products were examined using powder XRD. XRD patterns obtained from the $Gd(OH)_3$ and $Gd_2O_2S:Eu^{3+}$ products are shown in Fig. 1a, b, respectively. All peaks can be perfectly indexed as the pure hexagonal phase and they are in good agreement with standard $Gd(OH)_3$ ([$P6_{3/m}$, 176], JCPDS # 83-2037; Lattice constant: $a = b = 6.261$ Å, $c = 3.544$ Å) and $Gd_2O_2S:Eu^{3+}$, ([P3m1, 164], JCPDS # 27-1422; Lattice constant: $a = b = 3.784$ Å, $c = 6.589$ Å) data. It is observed that for the $Gd_2O_2S:Eu^{3+}$ nanostructures, there is a marginal decrease (~0.365%) in crystallographic unit-cell volume that tends to contract due to the increase in surface area of the crystallites. This may lead to a decrease in the lattice constant. No peaks attributable to other types of gadolinium hydroxide(s) and oxysulfide(s) are observed in the XRD patterns, indicating the high purity of the samples obtained.

The $Gd(OH)_3$ nanocrystals/nanoplates, nanosheets, nanobelts, nanotubes, nanorods, and nanowires are selectively synthesized were based on the preparation of colloidal hydroxide precipitates at room temperature, and the subsequent hydrothermal treatment at 100–180 °C for approximately 12–48 h. The hydrothermal method was shown to be effective in the synthesis of zero and one-dimensional nanostructures. By simply tuning the factors such as pH, temperature, and concentration, the experimental conditions could be chosen to favor the anisotropic growth of materials. In this article, nanostructures of $Gd(OH)_3$ were successfully obtained through this precipitation–hydrothermal synthetic method by properly tuning the temperature, pH, and the crystal structures have been found to be responsible for the growth of hydroxide nanostructures with nearly controllable aspect ratios. The optimal experimental conditions and resulting morphologies of $Gd(OH)_3$ nanostructures are given in Table 1.

Figure 2a–f shows the TEM, HRTEM, and electron diffraction measurements of the synthesized $Gd(OH)_3$ nanocrystals, nanosheets, nanobelts nanotubes, nanorods, and nanowires are seen to be single-crystalline in nature. The resulting morphologies and synthesis conditions of $Gd(OH)_3$ are discussed in Table 1. With the above-synthesized $Gd(OH)_3$ as possible precursor oxysulfide nanostructures were easily obtained by the sulfidation process. The shape-selective synthesis of the possible reaction mechanism of $Gd_2O_2S:Eu^{3+}$ nanostructures in the hydrothermal research is to control the crystal growth in a specific direction. The strategies in the morphology to control the growth of $Gd_2O_2S:Eu^{3+}$ nanocrystals/nanoplates, nanosheets, nanobelts, nanotubes, nanorods, and nanowires via hydrothermal route. The size and morphology of the products were further examined by transmission electron microscopy (TEM)/high-resolution TEM (HRTEM) in Fig. 3a–f are seen to be single-crystalline in nature. As can

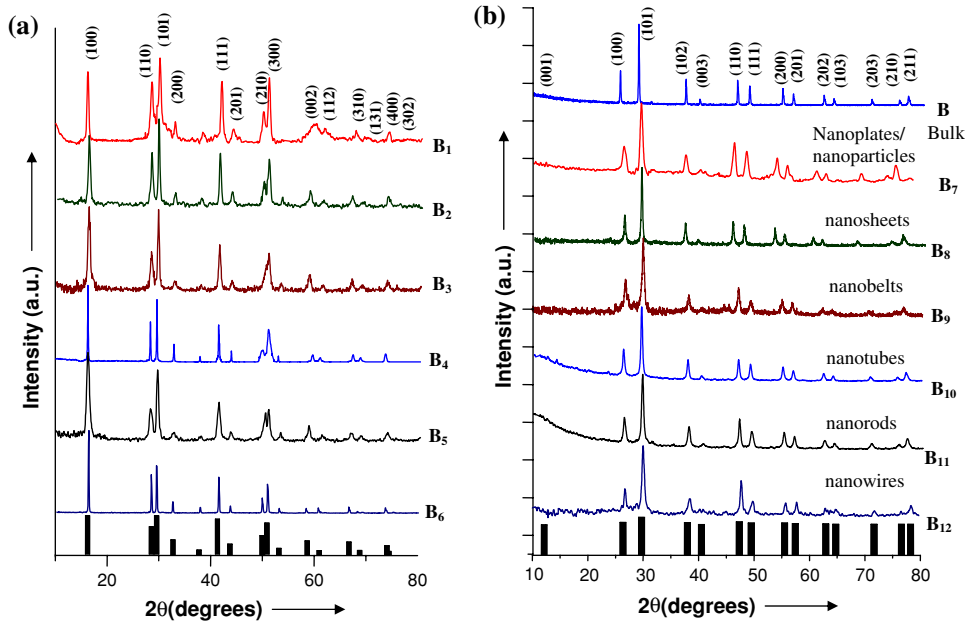

Fig. 1 **a** XRD patterns of the $Gd(OH)_3$ nanostructures: (B_1) Nanocrystals, (B_2) Nanosheets, (B_3) Nanobelts, (B_4) Nanotubes, (B_5) Nanorods, and (B_6) Nanowires. **b** XRD patterns of the $Gd_2O_2S:Eu^{3+}$ bulk and nanostructures: (B) Bulk, (B_7) Nanocrystals, (B_8) Nanosheets, (B_9) Nanobelts, (B_{10}) Nanotubes, (B_{11}) Nanorods, and (B_{12}) Nanowires obtained by hydrothermal treatment by varying the temperature and pH of the reaction mixture

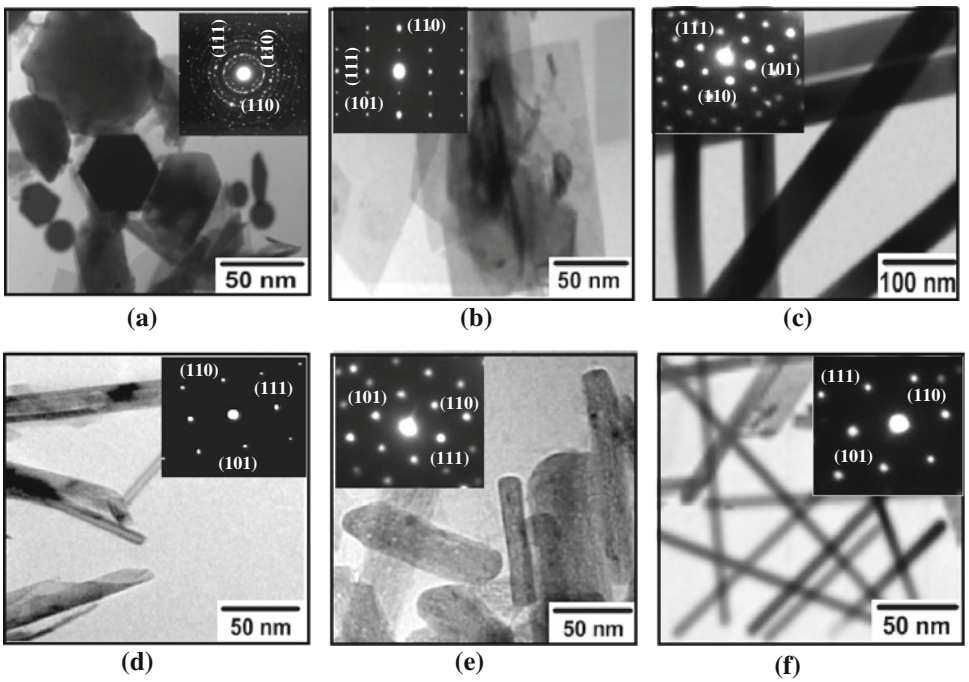

Fig. 2 Typical TEM images of $Gd(OH)_3$ nanostructures from the sample B_1 to B_6: **a** Nanocrystals, **b** Nanosheets, **c** Nanobelts, **d** Nanotubes, **e** Nanorods, and **f** Nanowires. All the samples are prepared according to the conditions presented in Table 1

be seen from the TEM images of Fig. 3a, that most of the nanoplates have a hexagonal morphology with sizes in the range 15–30 nm along with some agglomerated nature of spherical particles. Control experiments have been carried out to investigate the influence of pH value on the morphology of the final products. In the synthesis of $Gd_2O_2S:Eu^{3+}$ nanosheets are obtained when the pH value of the solution is maintained between 7 and 8 (Fig. 3b). While seeing these nanoplates and nanosheets are apparently the product of a mixed-shape evolution of 0D and/or 2D, 1D ripening, respectively [12]. The TEM image of Fig. 2c indicates the large quantity and good uniformity of the products of nanobelts can be seen to have uniform width over their entire lengths. The smooth, thin, beltlike structures have a width typically in the range of 30–50 nm and lengths of up to several tens to several hundreds of micrometers. These nanosheets and nanobelts curls from the edge, indicating a possible rolling process for the formation of the nanotubes. Hydrothermal methods have been shown to be effective in the synthesis nanosheets, nanobelts, nanotubes, nanorods, and nanowires [33, 34]. In contrast to synthetic strategies, such as the vapor–liquid–

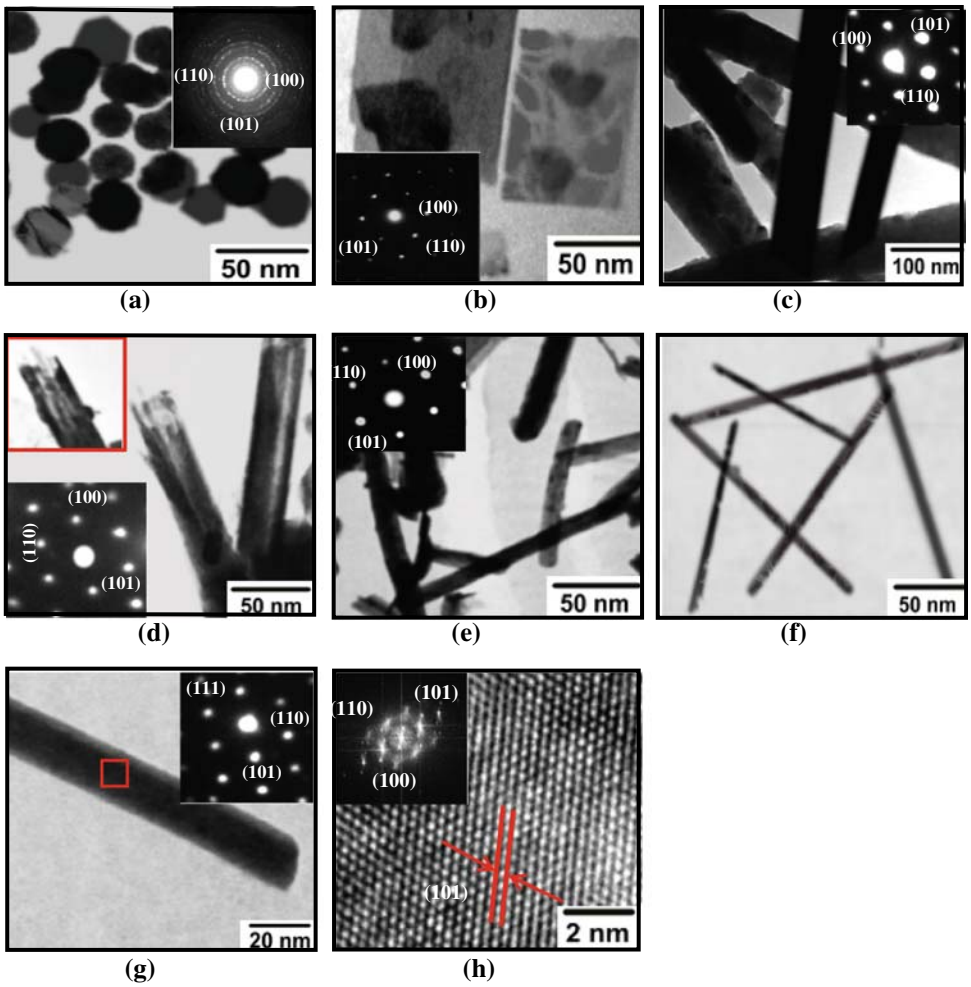

Fig. 3 The TEM images of $Gd_2O_2S:Eu^{3+}$ nanostructures from the sample B_7 to B_{12}: **a** Nanocrystals, **b** Nanosheets, **c** Nanobelts, **d** Nanotubes (inset: shows TEM image of the end portion of a single-nanotube), **e** Nanorods, **f** Nanowires, **g** a close-up of the boxed area in **f** shows a structure of single-nanowire, **h** HRTEM image of $Gd_2O_2S:Eu^{3+}$ nanowire. The spacing between two adjacent lattice planes is 0.325 nm, which corresponds to the separation of the hexagonal phase lattice planes (110), and the inset shows Fast Fourier transform (FFT) pattern of the corresponding nanowire

solid (VLS) or template-confined methods, the adopted synthetic method has no catalyst to serve as the energetically favorable site for the absorption of reactant molecules (VLS), and has no template to guide the directional growth of nanosheets, nanobelts, nanotubes, nanorods, and nanowires. Thus, it is reasonable to imagine that the driving force for the anisotropic growth of $Gd_2O_2S:Eu^{3+}$ nanostructures derives from the inherent crystal structure of $Gd(OH)_3$ materials and their chemical potential in solution. As shown in Fig. 3d, the central part of the cylindrical sample is white and the two peripheries are black, suggesting the formation of single nanotubes. The typical outer diameters of the nanotubes are in the range of 20–30 nm and the length of the nanotubes is estimated to be several nanometers in thickness. It is possible to see that in Fig. 3e the nanorods with a [110] growth direction thus suggesting the nanorods are grown along [110] direction. As followed by the optimal parameters from Table 1 the rest of hydroxide nanowires are controllably synthesized. The inset of Fig. 3a–f shows the electron diffraction pattern, which reveals that all the nanostructures are in single-crystalline phase and also stable enough to withstand the irradiation of convergent high-energy electron beam. Figure 3f, showing a high-magnification TEM image of $Gd_2O_2S:Eu^{3+}$ nanowires are single-crystalline in nature, are obtained after hydrothermal reaction for 48 h at 180 °C (Table 1). The images indicate the large quantity and good uniformity of the products. Also, based on the above studies, it was evident that these nanostructures are stable under thermal treatment, which may be rather useful for their applications in catalyst fields.

X-ray photoelectron spectroscopy (XPS) is known to study the composition and binding energy. This article discusses the XPS results only for the bulk and 1D nanowires of $Gd_2O_2S:Eu^{3+}$ as a comparison to identify the presence of elementary states of in the nano-oxysulfides. Figure 4a shows the wide-scan spectra of the hexagonal $Gd_2O_2S:Eu^{3+}$ bulk and 1D nanostructures in the range of 0–1350 eV, under identical conditions. Figure 4b–e shows the enlarged regions of the XPS spectra of the hexagonal $Gd_2O_2S:Eu^{3+}$ bulk and 1D nanowires, obtained in the range of 115–150 eV (Eu 4*d* at 128 eV and Gd 4*d* at

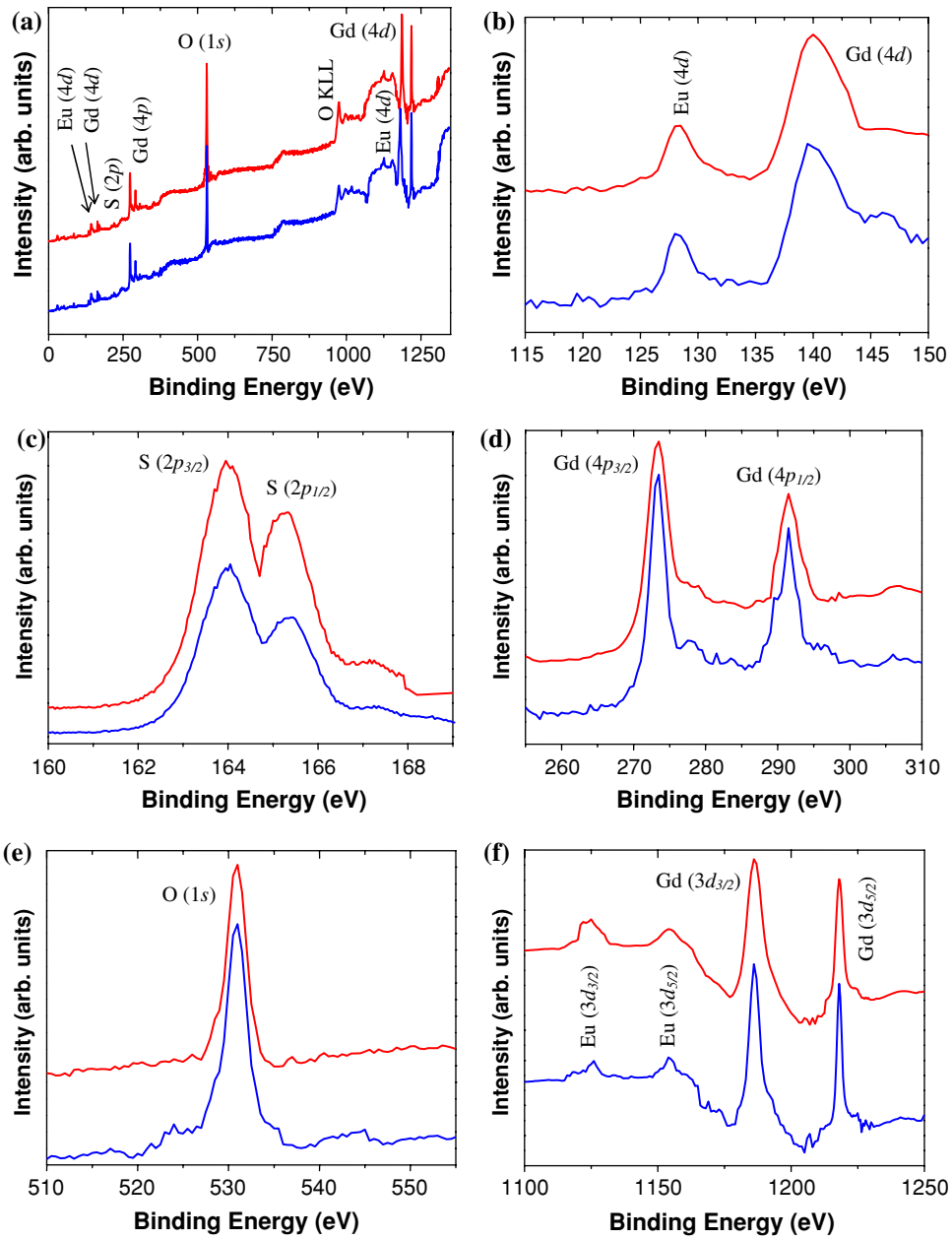

Fig. 4 XPS spectra of **a** complete XPS spectrum of $Gd_2O_2S:Eu^{3+}$ bulk and nanowires. Enlarged regions of the strong structure of XPS spectra **b** Gd(4*d*) and Eu(4*d*), **c** Sulfur (2*p*), **d** Gd (4*p*) and Eu (4*p*), **e** Oxygen (1*s*), **f** Gd (3*d*) and Eu(3*d*)

140 eV), 160–170 eV (S $2p_{3/2}$ at 164 eV and S $2p_{1/2}$ at 165.3 eV), 255–310 eV eV (Gd $4p_{3/2}$ at 273.5 eV and Gd $4p_{1/2}$ at 291.5 eV), 510 – 560 eV eV (O 1*s* at 531 eV), respectively, under identical conditions. Figure 4f shows the most intense photoelectron binding energy peaks are the ones at 1186, 1219 eV and 1126, 1154 corresponding to Gd ($3d_{5/2}$), Gd ($3d_{3/2}$) and Eu ($3d_{5/2}$), Eu ($3d_{3/2}$), respectively. All these peaks are in good agreement with the literature [35]. The Eu 4*d*, Gd 4*d*, and S 2*p* peaks are slightly weak as compared with that of the other major lines. The composition estimated by XPS using the relative sensitivity factors of Y, O, S, and Eu also revealed excess oxygen in the samples.

PL properties and FTIR studies of $Gd_2O_2S:Eu^{3+}$ nano/quantum structures

Figure 4a, b [10] shows a spatial electronic state diagram showing that the change in size of the nanostructures and the surface state relaxation process could be explained through a model energy level diagram of the europium in oxysulfide nanostructures, are illustrated, respectively. As the cluster properties are intermediate between nanoscale and bulk semiconductors, the size dependent effect can best be explained with semiconductor. Recent works are focuses on the preparation of nanostructured materials and their subsequent luminescent [10]. Owing to the clear change in

size dependent effects of nanomaterials because of their abnormal behavior and in tailoring the properties of these materials, which mainly come from the high surface/volume ratio in nanosystems. This may offer deep insight for understanding the important physical and chemical phenomena and as well as the quantum confinement effect. PL excitation spectra of bulk and nanostructures of $Gd_2O_2S:Eu^{3+}$ samples are shown in Fig. 5a. It is important to mention that luminescence data related to nanocrystals/nanoplates, nanosheets, nanobelts, nanotubes, nanorods, and nanowires of the doped oxysulfide systems show some interesting results. The spectral blue-shift in the excitation bands for the nanostructures from the bulk can be rationalized by considering them may be attributed to the quantum confinement effect especially in nanocrystals, nanotubes, nanorods, and nanowires when compared with the respective TEM images. The PL excitation spectra of the $Gd_2O_2S:Eu^{3+}$ system essentially comprising two parts viz., fundamental absorption band (~260 nm) and Eu^{3+}–X^{2-} ligand (X = O/S) CTB (~330 nm) show significant blue shifts, respectively, with respect to the bulk counterpart. Furthermore, from Fig. 6a, the blue-shift observed in the optical spectra has been proved through the diffuse reflectance spectra (converted to Kubelka-Munk plot) for the $Gd_2O_2S:Eu^{3+}$ nanostructures. The blue-shift in the optical spectra for the oxysulfide system corresponding to the fundamental absorption band and Eu^{3+}–X^{2-} ligand (X = O/S) CTB show significant blue shifts (~0.22–0.36 eV), respectively, with respect to the bulk counterpart. These may be explained by considering possible size dependent changes in this wide bandgap semiconductor system.

In luminescent material field, phosphors-based gadolinium compounds play an important intermediary role because the Gd^{3+} ion ($4f^7$, ^8S) has its lowest excited levels at relatively high energy (>32,000 cm^{-1}) due to the stability of the half-filled shell ground state [36]. The fluorescence of rare-earth ions mainly originates from electron transitions within the 4f shell. Trivalent Gd has a half-filled 4f shell and the realization of any *f–f* transitions would involve the breaking of the stable $4d^{10}4f^7$ configuration. As a result, the transition energy for *f–f* transitions of Gd^{3+} is much higher than for other Ln^{3+} with partially filled 4f shells, and also can serve as a host material. Generally, the PL emission spectrum (Fig. 5b) of Eu^{3+}-doped Gd_2O_2S (λ_{exc} = 330 nm) consists of sharp lines ranging from 575 to 710 nm, respectively. The emission transitions which are associated from the excited level of $^5D_0$ to the levels of ^7F_J (J = 1, 2, and 4) of Eu^{3+} [37], respectively. Among several luminescence transitions of Eu^{3+}, the $^5D_0 \rightarrow {}^7F_1$ (~590 nm) emission transition is mainly magnetically allowed (a magnetic-dipole transition). It is structure independent, while $^5D_0 \rightarrow {}^7F_2$ (626 nm) and $^5D_0 \rightarrow {}^7F_4$ (~700 nm) are hypersensitive forced and weak electric-dipole transitions, respectively, being allowed only

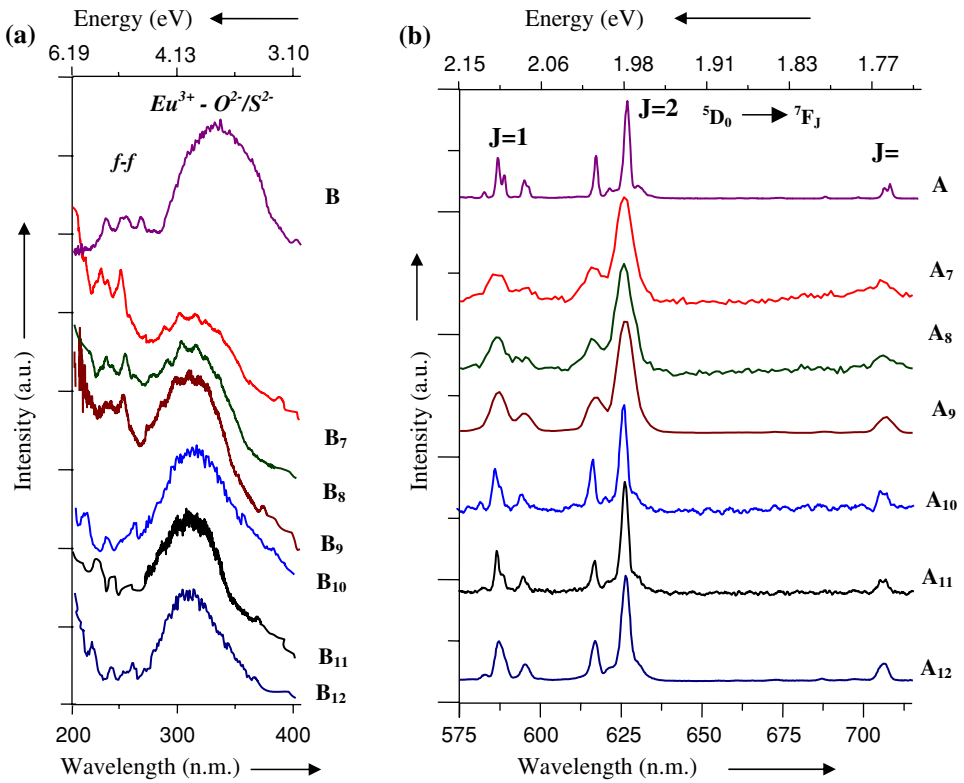

Fig. 5 **a** shows the $GdO_2S:Eu^{3+}$ room temperature photoluminescence excitation spectra (λ_{em} = 626 nm) of bulk and nanostructures. *f–f* indicates Eu^{3+} lines from higher levels and CTB indicates the Eu^{3+}–ligand charge transfer band. **b** Photoluminescence emission spectra (λ_{exc} = 330 nm) corresponding to various $^5D_0 \rightarrow {}^7F_J$ (J = 1, 2, 4) transitions revealing identical Stark-splitting patterns for both bulk and nanostructures with respect to the variation in concentration of the samples

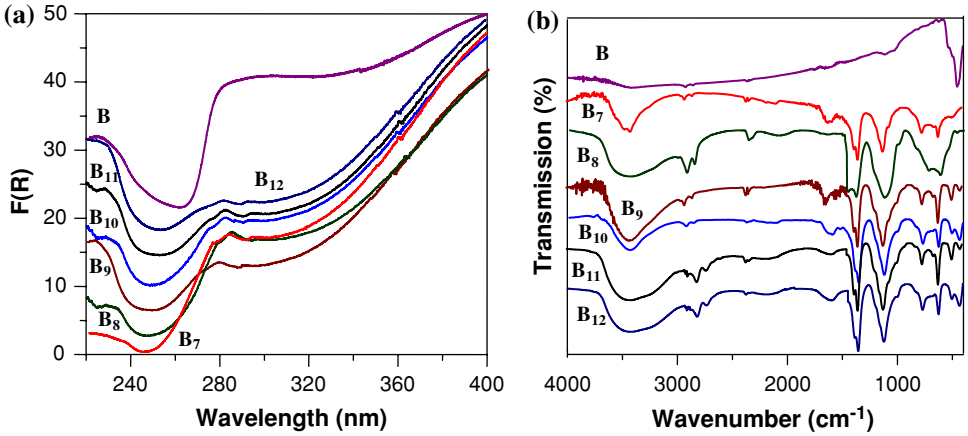

Fig. 6 **a** Kubelka-Munk plot for bulk (B) and nanocrystals to nanowire (B_7 to B_{12}) $Gd_2O_2S:Eu^{3+}$ samples converted from reflectance spectra. **b** FTIR spectra of bulk (B) and nanocrystals to nanowire (B_7 to B_{12}) $Gd_2O_2S:Eu^{3+}$ samples

at low symmetries with no inversion center. These transitions are known to be hypersensitive to crystal-structure and chemical surroundings [10]. A moderately resolved PL emission spectrum and the corresponding Stark splitting pattern of $^5D_0 \rightarrow {}^7F_J$ ($J = 0$–2) and intra-configurational *f*–*f* electronic transitions of Eu^{3+}-doped Gd_2O_2S nanostructures indicate a close comparison with the bulk counterpart. This may suggest nearly identical chemical surroundings for the Eu^{3+} center (C_{3V} symmetry) in both cases. Whereas, excitation processes between bulk and nanosamples will be different due to the presence of innumerable surface state(s) in the latter.

The highly reactive nature of the porous nanoparticles will show a pronounced propensity to chemisorbed gases that may have evolved during the course of the nanocrystal synthesis. On comparison of the FTIR spectra (Fig. 6b) of $Gd_2O_2S:Eu^{3+}$ bulk (B) and nanostructures (B_7 to B_{12}), it is obvious that the nanostructures show absorption around 3500 and 1500 cm^{-1}. Although, the absorption in these regions corresponds to ammonium/cyano-amine groups, the presence of the hydroxyl group due to contamination of the nanoparticles by moisture also should be considered. Owing to large surface area and porosity of nanocrystals different gases (CO_2, NH_3, SO_2, SO_3, H_2O, etc.,) evolved during thermolysis, may get chemisorbed which may be reflected in the FTIR spectra. FTIR spectrum of the $Gd_2O_2S:Eu^{3+}$ nanostructures showed pronouncing features in the region of 600–1700 cm^{-1}. Intense absorption peaks in the regions around 600, 1100, 1400, and 3500 cm^{-1} may signify the presence of [ν(Y/Eu–O), δ(Y–S)], δ(S–O), ν(C–O), and δ (O–H) modes, respectively [38], in particular suggesting a significant modification in the stretching mode(s) of (Y/Eu–O) complex. For semiconductor nanocrystals, the shift in the position of lowest vibrational state ($\nu = 0$) of the excited state with respect to that corresponding to the ground state can be given by influence of possible modification in acoustic/optical modes [39], which may also come as the result of difference in chemisorbed species between bulk and nanocrystalline samples.

Opto-impedance analysis on $Gd_2O_2S:Eu^{3+}$ nanostructures

The surfaces of semiconductor nanostructures play an important role in determining their optical properties. Relaxation of surface states (SS) with the combination of electric-field resonance and their role in augmenting various photo-chemical properties, such as electro-luminescence, solar cells, etc., have been well-demonstrated [10, 40, 41]. In opto-impedance spectroscopy, Nyquist plot is of more practical significance especially when employed for nanomaterial characterization. In order to identify the origin and nature of the electronic transitions observed in the visible region, the opto-impedance measurements for these samples both under UV exposure (254 and 365 nm radiation) and without UV (dark) conditions were made. Figures 7a–d and 8a, b, show the Nyquist type impedance plot of Eu^{3+}-doped Gd_2O_2S bulk and nanostructures. Nyquist type impedance plot shows a simple semicircle, accompanied by a small semicircle with an adjoining straight line (Warburg pattern). Detailed discussions related to Warburg impedance processes are already studied [10]. Furthermore, the studies related to other various nanostructures are reported here. It should be noted that from the opto-impedance process, the magnitude of charge carriers, (i.e., the total charge) associated with surface states as reflected in the opto-impedance data can be obtained from the relation.

$$e_0 N_{ss} = Q_{ss} = \int_{V_0}^{V_1} C_{ss} dV \quad (1)$$

From Table 2, the optical excitation causes substantial increase in both R_{SS} and C_{SS} values corresponding to resistance and capacitance values of surface-states

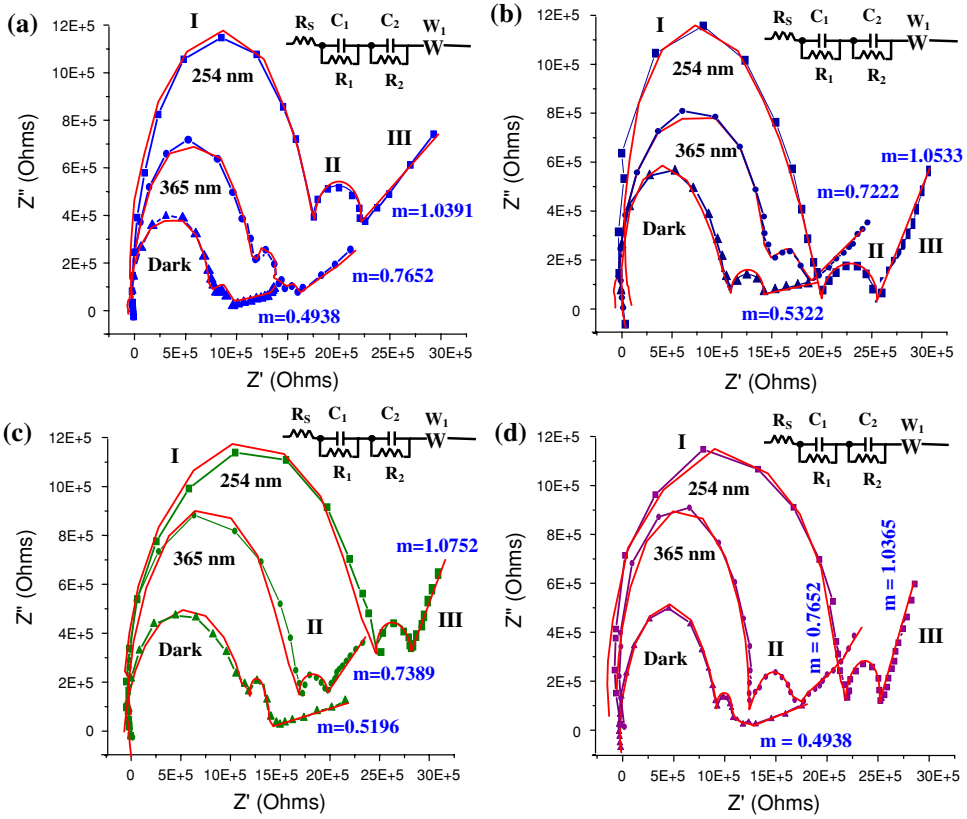

Fig. 7 Nyquist impedance fitted plot of $Gd_2O_2S:Eu^{3+}$ nanostructures: **a** Nanocrystals, **b** Nanosheets, **c** Nanobelts, **d** Nanotubes, according to Table 1, under dark and UV excitation conditions (254 and 365 nm) and the corresponding electrical-impedance equivalent circuits. The regions I, II, and III represents the semi-circles (of RC parallel network, relaxation of surface-states) and Warburg impedance pattern upon UV shining in the nano-systems

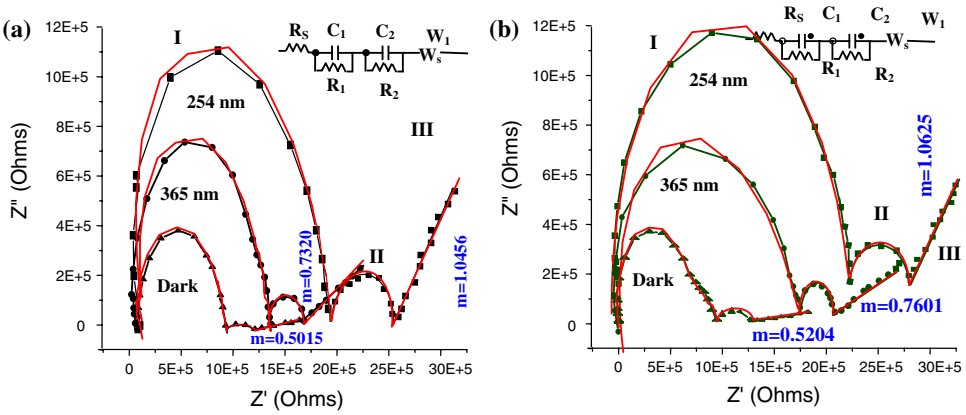

Fig. 8 Nyquist impedance fitted plot of $Gd_2O_2S:Eu^{3+}$ nanostructures: **a** Nanorods, **b** Nanowires under dark and UV excitation conditions (254 and 365 nm) and the corresponding electrical-impedance equivalent circuits. Warburg impedance pattern with variation in slope (m) upon UV shining

suggesting significant increase in photo-generated carriers. This may stem from photo-induced relaxation of surface sates. As a result, UV exposure influences the surface state relaxation in these nanoscale materials. This can in turn influence the ligand to metal charge transfer transitions of Eu^{3+}-doped gadolinium oxysulfide nanostructured materials. Further studies are being performed concerning the novel properties and exploration for application of these nanostructures, such as catalytic, optoelectronic, magnetic, biological, and luminescence properties. It is estimable that these novel low-dimensional functional nanostructures with different shapes and sizes will provide further research opportunities in chemistry, physics, and other interdisciplinary fields of science and technology. Hence, the results provide an effective route to synthesize oxysulfide nanostructures and are helpful for investigating the optic characters in the nanostructures, and promote the potential biomedical and display applications in oxysulfide nanophosphors.

Conclusion

We have bequeathed a simple and safe hydrothermal route that can control the shape of $Gd_2O_2S:Eu^{3+}$ nanostructures. Highly crystalline $Gd_2O_2S:Eu^{3+}$ nanocrystals/nanoplates,

Table 2 Warburg impedance parameters values of $Gd_2O_2S:Eu^{3+}$ nanostructured system

Morphology and sample	UV condition	$R_{sc} \times 10^6$ (Ωcm^2)	C_{sc} (μF)	R_{ss} (Ω cm^2)	C_{ss} (μF)	WsR $\times 10^6$ (Ωcm^2)	WsT (s)	WsP
Nanocrystals (B_7)	254 nm	2.59	1.72E−11	323710	1.65E−8	4.25	86.34	0.4575
	365 nm	2.19	1.60E−11	308541	2.55E−8	3.45	73.32	0.3780
	No UV	1.73	2.05E−11	278535	7.45E−9	1.59	12.62	0.2602
Nanosheets (B_8)	254 nm	2.52	1.91E−11	335746	1.86E−8	4.13	90.87	0.4794
	365 nm	2.13	1.82E−11	301989	2.71E−8	3.54	76.77	0.3412
	No UV	1.82	1.90E−11	248256	7.25E−9	1.50	10.15	0.2565
Nanobelts (B_9)	254 nm	2.46	1.95E−11	388989	1.82E−8	4.01	95.84	0.4644
	365 nm	2.16	1.77E−11	309621	2.60E−8	3.35	74.89	0.3474
	No UV	1.85	1.95E−11	278550	7.45E−9	1.52	10.15	0.2565
Nanotubes (B_{10})	254 nm	2.54	1.84E−11	354725	1.77E−8	4.28	96.06	0.4885
	365 nm	2.16	1.62E−11	306458	2.65E−8	3.72	76.74	0.3834
	No UV	1.85	2.03E−11	265425	6.46E−9	1.65	12.28	0.2685
Nanorods (B_{11})	254 nm	2.50	1.80E−11	386725	1.74E−8	4.08	89.14	0.4865
	365 nm	2.12	1.55E−11	305461	2.21E−8	3.44	76.19	0.3768
	No UV	1.98	2.09E−11	225350	6.89E−9	1.52	11.67	0.2660
Nanowires (B_{12})	254 nm	2.56	1.92E−11	385647	1.86E−8	4.05	94.98	0.4844
	365 nm	2.16	1.82E−11	306621	2.58E−8	3.57	77.89	0.3284
	No UV	1.85	1.95E−11	275250	7.20E−9	1.59	10.33	0.2585

R_{SS} and C_{SS} indicate resistance and capacitance values of surface-states. Different Warburg parameters WsR (Ω), WsT (s), WsP indicate bulk (ohmic) resistance, Warburg resistance, Warburg time constant, and order of the process, respectively

nanosheets, nanobelts, nanotubes, nanorods, and nanowires were selectively synthesized without any additives under ambient conditions. Room temperature PL spectra showed that, the $Gd_2O_2S:Eu^{3+}$ nanostructures showed a significant blue-shift in both the fundamental absorption edge and Eu^{3+}–X^{2-} (ligand X = O/S) charge transfer (excitation) bands. The opto-induced impedance studies indicate that the energy dependent shift in the slope of the Warburg impedance pattern is regulated by a diffusion mechanism and increases the capacitive-impedance. This has been related to photo-induced modification in surface state relaxation processes and which are absent in the bulk system.

Acknowledgements One of the authors J. Thirumalai wishes to thank the Director of Collegiate Council, Chennai for providing fellowship and gratefully thank NIIST (CSIR), Trivandrum, IGCAR, Kalpakkam, IIT–Bombay, Mumbai, and IICT (CSIR), Hyderabad for extending instrumentation facilities.

References

1. Alivisatos AP (1996) Science 271:933
2. Xia Y, Yang P, Sun Y, Wu Y, Mayers B, Gates B, Yin Y, Kim F, Yan H (2003) Adv Mater 15:353
3. Zhang J, Sun L, Yin J, Su H, Liao C, Yan C (2002) Chem Mater 14:4172
4. Geng J, Lu D, Zhu J, Chen H (2006) J Phys Chem B 110:13777
5. Tang Q, Zhou WJ, Ou SM, Jiang K, Yu WC, Qian YT (2005) Cryst Growth Des 5:147
6. Liu ZP, Peng S, Xie Q, Hu ZK, Yang Y, Zhang SY, Qian YT (2003) Adv Mater 15:936
7. Xie G, Qiao ZP, Zeng MH, Chen XM, Gao SL (2004) Cryst Growth Des 4:513
8. Wang H, Zhu JJ, Zhu JM, Chen HY (2002) J Phys Chem B 106:3848
9. Thirumalai J, Chandramohan R, Sekar M, Rajachandrasekar R (2008) J Nanopart Res 10:455
10. Thirumalai J, Chandramohan R, Divakar R, Mohandas E, Sekar M, Parameswaran P (2008) Nanotechnology 19:395703
11. Nakkiran A, Thirumalai J, Jagannathan R (2007) Chem Phys Lett 436:155
12. Peng ZA, Peng XG (2001) J Am Chem Soc 123:1389
13. Wang X, Li Y (2003) Chem Eur J 9:5627
14. Royce MR (1968) US Patent Specification 3(418):246
15. Yeboah C, Pistorius S (2000) Med Phys 27:330
16. Raukas M, Mishra KC, Peters C, Schmidt PC, Johnson KH, Choi J, Happek U (2000) J Lumin 87–89:980
17. Kong YC, Yu DP, Zhang B, Fang W, Feng SQ (2001) Appl Phys Lett 78:407
18. Xu CX, Sun XW, Dong ZL, Yu MB (2004) Appl Phys Lett 85:3878
19. Huang MH, Mao S, Feick H, Yan H, Wu Y, Kind H, Weber E, Russo R, Yang P (2001) Science 292:1897
20. Johnson JC, Yan H, Yang P, Saykally RJ (2003) J Phys Chem B 107:8816
21. Kind H, Yan H, Messer B, Law M, Yang P (2002) Adv Mater 14:158
22. Wan Q, Li QH, Chen YJ, Wang TH, He XL, Li JP, Lin CL (2004) Appl Phys Lett 84:3654
23. Pan ZW, Dai ZR, Wang ZL (2001) Science 291:1947
24. Law M, Greene LE, Jhonson JC, Saykally R, Yang P (2005) Nat Mater 4:455
25. Zhang BP, Binh NT, Wakatsuki K, Segawa Y, Yamada Y, Usami N, Kawasaki M, Koinuma H (2004) Appl Phys Lett 84:4098

26. Wang BG, Shi EW, Zhong WZ (1998) Cryst Res Technol 33:937
27. Jun YW, Lee SM, Kang NJ, Cheon J (2001) J Am Chem Soc 123:5150
28. Fang YP, Xu AW, You LP, Song RQ, Yu JC, Zhang HX, Li Q, Liu HQ (2003) Adv Funct Mater 13:955
29. Wang X, Sun X, Yu D, Zou B, Li YD (2002) Adv Mater 41:1442
30. Suslick KS, Fang M, Hyeon T (1996) J Am Chem Soc 118:11960
31. Yu JC, Yu J, Ho W, Zhang L (2001) Chem Commun 1942
32. Dhas NA, Suslick KS (2005) J Am Chem Soc 127:2368
33. Wang X, Li YD (2002) J Am Chem Soc 124:2880
34. Li YD, Wang JW, Deng ZX, W u YY, Sun XM, Yu DP, Yang PD (2001) J Am Chem Soc 123:9904
35. Moulder JF, Stickle WF, Sobol PE, Bomben KD (1992) In: Chastain J (ed) Handbook of X-ray photoelectron spectroscopy. Perkin-Elmer Corporation, Eden Prairie, MN
36. Blasse G (1992) Phys Status Solidi A 130:K85
37. Bang J, Abboudi M, Abrams B, Holloway PH (2004) J Lumin 106:177
38. Nakamoto K (1997) Infrared and Raman spectra of inorganic coordination compounds, 5th edn. John Wiley & Sons, New York
39. Heath JR, Shiang JJ (1998) Chem Soc Rev 27:65
40. Bisquert J (2002) Electrochimica Acta 47:2435
41. Bockris JÓM, Khan SUM (1993) Surface electrochemistry: a molecular level approach. Plenum Press, New York